nature materials

ARTICLES

https://doi.org/10.1038/s41563-019-0296-5

Nonlinear photoresponse of type-II Weyl semimetals

Junchao Ma[1], Qiangqiang Gu[1], Yinan Liu[1], Jiawei Lai[1], Peng Yu[2], Xiao Zhuo[1], Zheng Liu[2], Jian-Hao Chen[1,3]*, Ji Feng[1,3,4]* and Dong Sun[1,3]*

The experimental manifestation of topological effects in bulk materials is attracting enormous research interest. However, direct experimental evidence of the effective *k*-space monopole of the Weyl nodes has so far been lacking. Here, signatures of the singular topology of the type-II Weyl semimetal $TaIrTe_4$ are revealed in the photoresponses, which are related to divergence of the Berry curvature. $TaIrTe_4$ exhibits a large photoresponsivity of 130.2 mA W^{-1}—with 4 μm excitation in an unbiased field-effect transistor at room temperature—arising from the third-order nonlinear optical response, approaching the performance of commercial low-temperature detectors. In addition, the circularly polarized galvanic response is enhanced at 4 μm, possibly due to the same Berry curvature singularity enhancement. Considering the optical selection rule of chiral Weyl cones, this may open the door for studying and controlling the chiral polarization of Weyl fermions with an electric field in addition to the optical helicities.

The exploration of topological effects, which have useful and unique applications in condensed matter materials, is attracting a lot of interest[1–4]. The quantum Hall system is a patent manifestation of the topological effect in the insulating phase, which, as well as its fundamental significance, has found practical application as a metrological standard for resistance. The recently discovered Weyl semimetals (WSMs), belonging to the class of topological metallic phases, provide an ideal platform to explore the physical effects that relate to topology in gapless materials[5–11]. Surface Fermi arcs and the chiral anomaly, characteristics of Weyl fermions, have been widely used for the experimental verification of WSMs through angle-resolved photoemission spectroscopy (ARPES)[6,7,12,13] and transport measurements[14–16], respectively. The defining feature of a WSM is the divergence of Berry curvature at the Weyl nodes, leading to topological semi-metallic phases. The divergence behaves like the magnetic monopoles of momentum space, and the sign of the monopole determines the chirality. On the other hand, nonlinear optoelectronic responses play a crucial role not only in optical devices but also in probing the fundamental properties of quantum materials. Although a nonlinear optical process that involves direct optical transitions to high-energy excited states may not directly capture the low-energy singularity at the Weyl nodes, its measurable effect, such as the photocurrent response, will involve the ground and low-energy excited states that are characterized by the geometric and topological nature of the Bloch wavefunctions at the nodes. These ground and low-energy excited state properties of Weyl nodes involve the singularity of the Berry curvature, an intrinsic geometric property of Bloch wavefunctions, which plays an essential role in the transport phenomena of photoexcited carriers. It has been proposed theoretically that the singular Berry curvatures at the Weyl nodes could be manifested in a macroscopic nonlinear optical response such as second harmonic generation[17] and the photocurrent response through shift vectors[18–20]. The shift current is the photocurrent generated due to a change in the centre of mass upon optical excitation[21,22]. It is considered a promising candidate responsible for the high-efficiency photovoltaic current in solar cells without a p–n junction[23–27]. The shift current response is related to the geometric effects associated with the Berry connection and curvature of the Bloch bands, which in turn form the basis for defining the topology in band structures[18,28]. Furthermore, theoretical investigations show a stark contrast in the low-frequency dependence of the shift current response in type-I and type-II WSMs: the shift current diverges in the low-frequency $\omega \to 0$ limit for a type-II WSM, but vanishes ($\propto\omega$) for a type-I WSM with zero doping[28]. In this Article we experimentally demonstrate the manifestation of the divergent Berry curvature of Weyl nodes in the giant mid-infrared photoresponse of $TaIrTe_4$, a type-II WSM. Our calculations of the third-order nonlinear response indicate that the shift current generation involves a significant contribution from the singular feature of the Weyl nodes. Taking advantage of the Berry curvature singularity enhancement being similar to that of the shift current, we further demonstrate that the third-order nonlinear injection current terms may provide additional control for the optical injection of chiral carriers in the Weyl cones through an in-plane electric field.

Our experiment is based on the layered orthorhombic ternary compound tantalum iridium tetratelluride ($TaIrTe_4$), which hosts four well-separated type-II Weyl nodes, the minimum number imposed by symmetry in a WSM without inversion symmetry. It offers a 'hydrogen atom' example of an inversion-breaking WSM[29]. In addition, $TaIrTe_4$ also hosts larger Fermi arc surface states and inherits all the advantages of a layered material, such as the ability to form van der Waals heterostructures with other two-dimensional (2D) layered materials[30]. The $k_c = 0$ cross-section of the Brillion zone harbours all four Weyl nodes. The 3D band structures of Weyl cones are shown in Fig. 1a–d. The three crystallographic axes are referred to as a, b and c, as shown in Fig. 1e; accordingly, the three components of a wavevector are denoted k_a, k_b and k_c, respectively. The four Weyl cones can be mapped exactly onto each other through mirror and time reversal symmetry. In the k_a direction, the bands are strongly tilted to form type-II Weyl cones, while along the k_b direction the bands are almost upright (Supplementary section I). The theoretically predicted Fermi level lies about 80 meV below the Weyl nodes. For this reason, the Weyl nodes are not conveniently

[1]International Center for Quantum Materials, School of Physics, Peking University, Beijing, China. [2]School of Materials Science and Engineering, Nanyang Technological University, Singapore, Singapore. [3]Collaborative Innovation Center of Quantum Matter, Beijing, China. [4]CAS Center for Excellence in Topological Quantum Computation, University of Chinese Academy of Sciences, Beijing, China. *e-mail: chenjianhao@pku.edu.cn; jfeng11@pku.edu.cn; sundong@pku.edu.cn

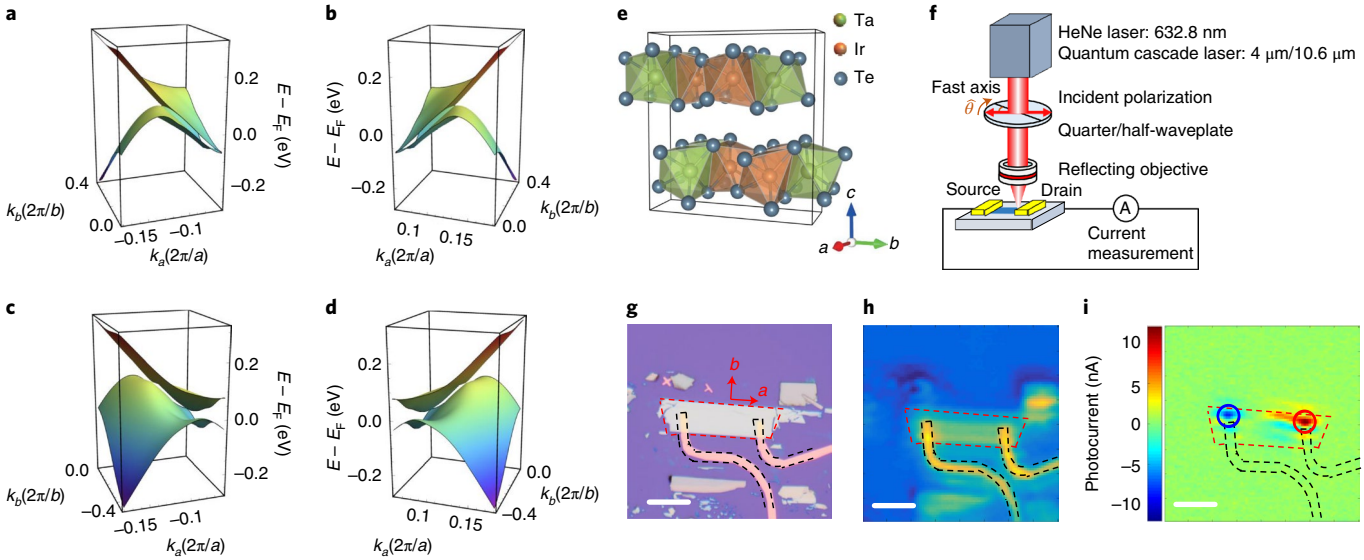

Fig. 1 | Type-II WSM $TaIrTe_4$ and scanning photocurrent response. a–d, Band structure of $TaIrTe_4$ in the vicinity of four Weyl nodes in the Brillouin zone, where **a** (**d**) and **b** (**c**) correspond to opposite chiralities. k_a and k_b are reciprocal lattice vectors. **e**, Crystal structure of $TaIrTe_4$ with three crystallographic axes (*a*, *b* and *c*). **f**, Schematic diagram of the polarization-resolved scanning photocurrent measurement set-up. **g**, Optical microscopy image of the device. The device is at the centre, outlined by the red dashed line, with a pair of gold electrodes outlined by black dashed lines. Some other exfoliated $TaIrTe_4$ flakes are located around the device. The crystallographic *a* and *b* axes are marked by red arrows. **h**,**i**, Scanning reflection and photocurrent images of the $TaIrTe_4$ device at room temperature with 4 μm linear polarized light along the crystallographic *a* axis. The excitation power is 490 nW. The maximum photocurrent responses are 12.45 nA and −8.49 nA. Scale bars, 20 μm.

accessible in conventional transport and ARPES measurements without a special experimental arrangement to tune the Fermi level over an extremely large energy range[13]. However, with suitable photon energy and through photogalvanic effect measurements, the Weyl properties are demonstrated to be accessible by the photon probe in this work[31].

A schematic diagram of the photocurrent measurement is provided in Fig. 1f: continuous-wave light sources with different wavelengths are polarization-controlled and focused on a specific position on a lateral metal–$TaIrTe_4$–metal device (Fig. 1g). Throughout this Article we use normal-incidence light and we assign $-\hat{\mathbf{c}}$ as the direction of propagation of the light. Scanning reflection and photocurrent images excited with 4 μm linear polarization along the crystallographic *a* axis (LP-a) are shown in Fig. 1h and 1i, respectively. The response pattern is qualitatively the same with a higher-spatial-resolution scanning image at 633 nm (Supplementary Section II), and the results indicate that the photoresponse is not only limited to the interface between the metal contacts but also extends to regions far away from the contact. The scanning photocurrent response pattern is determined by multiple factors, including thickness, doping profile and field line distribution between the contacts, which is a result of the interplay of multiple photocurrent generation mechanisms.

Figure 2a shows the power dependence of the photoresponse for different excitation wavelengths (more data on other devices are provided in Supplementary Section III). While the photoresponses at 633 nm, 1.5 μm and 10.6 μm are linear with excitation power, the response at 4 μm is strikingly different in the low-power region. In comparison with the responsivity of 22.4 μA W^{-1} in the high-power region, the responsivity in the low-power region is more than three orders of magnitude larger, reaching a maximum slope of 130.2 mA W^{-1}, as shown in Fig. 2b. Here, we note that there is a 'turn on' threshold at low excitation power (~155 nW for LP-a and ~192 nW for LP-b), which corresponds to the minimum excitation power required to circumvent the potential barriers in the measurement system so that a measurable photocurrent is induced. This turn on threshold is related to the interplay of multiple potential barriers in the measurement circuit and cannot be removed by simply adding a fixed bias during the measurement before reaching the damage threshold of the device (Supplementary Section IV). Figure 2b further shows the power dependence for different excitation polarizations at 4 μm. The response has a polarization dependence. First, with LP-a excitation, the photoresponse is much larger than that with linear polarization along the crystallographic *b* axis (LP-b). The response is highly anisotropic, and the long axis of the ellipse of the anisotropic response is consistent with the crystallographic *a* axis (Fig. 2c). The anisotropy ratio, which is defined as the ratio of the photocurrent response with LP-a excitation to that with LP-b excitation, increases monotonically as the excitation power decreases (Fig. 2d). Due to the limit imposed by the turn on threshold, the plot in Fig. 2d is cut at the power when the response of LP-b excitation reaches the noise floor (~200 nW). On the other hand, the response to the left circular polarization (LCP) excitation is larger than that to the right circular polarization (RCP) excitation, which corresponds to circular photogalvanic effect (CPGE).

Our calculation shows that the photoresponsivity at 4 μm involves a significant shift current response, which in turn can arise from the diverging Berry curvature at the Weyl nodes, as predicted by recent theory[18,19,28]. Here, an analysis of the nonlinear photocurrent tensor σ_{shift}, which is responsible for the shift current generation, is offered in accordance with the crystal symmetry. An approximate calculation of the shift current tensor in $TaIrTe_4$ affords a semi-quantitative analysis of the experimentally observed giant photoresponse. As will be shown, the computed σ_{shift} does involve a significant contribution from the divergence of geometric quantities near the Weyl nodes.

It has been demonstrated experimentally that the shift current response from a type-I Weyl cone results in a glass coefficient that is an order of magnitude larger than other previously measured values[19]. Interestingly, the observed giant shift current response in $TaIrTe_4$ is a result of a third-order nonlinear effect. The rank-3 tensor $\sigma_{(2)}^{\alpha\beta\gamma}$ for the in-plane d.c. optical response vanishes for $\alpha,\beta,\gamma = a,b$ (in the plane of the device and perpendicular to the direction of the

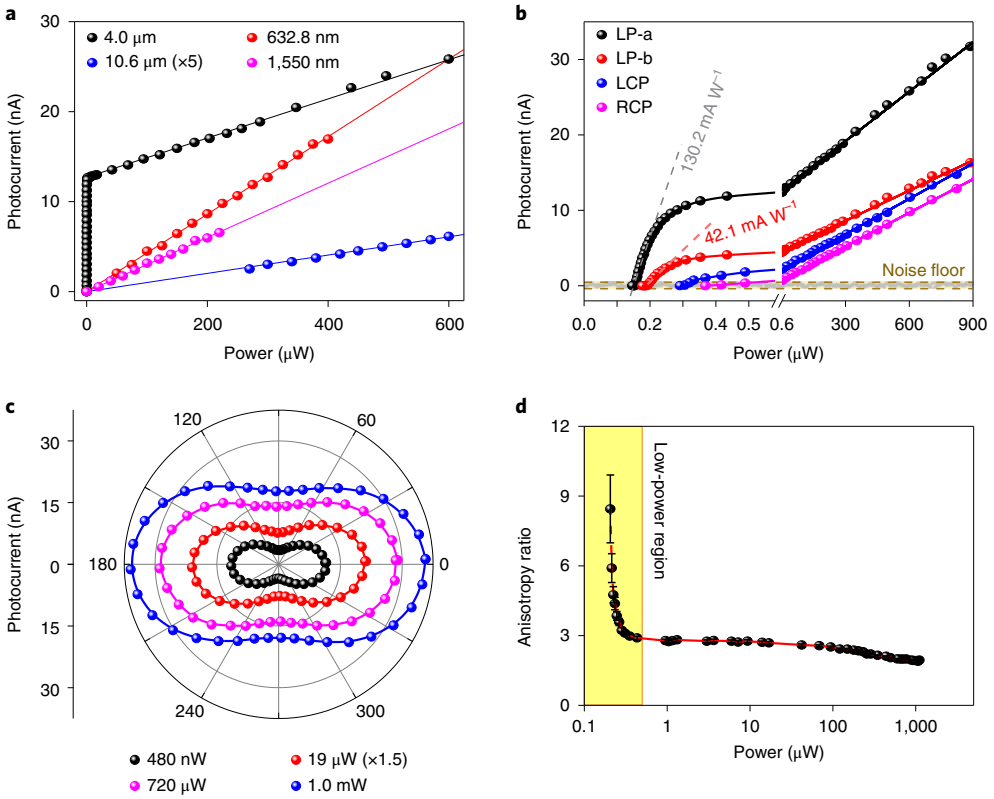

Fig. 2 | Giant and anisotropic shift current response. a, Excitation power dependence of the photocurrent response at different wavelengths at a fixed excitation spot (marked by the red circle in Fig. 1i). The responsivities for 632.8 nm, 1,550 nm and 10.6 μm excitations are 43.05 μA W^{-1}, 30.13 μA W^{-1} and 2.03 μA W^{-1}, respectively. All the excitations are linearly polarized. **b**, Excitation power dependence of the photocurrent response at 4 μm excitation linearly polarized along the *a* axis (LP-a), *b* axis (LP-b), RCP and LCP excitations, respectively. Grey and red dashed lines show the linear fittings of responsivities 130.2 mA W^{-1} and 42.1 mA W^{-1} of linear regions at low excitation power with LP-a (from 155.33 nW to 206.1 nW) and LP-b (from 192.35 nW to 246.54 nW) excitation, respectively. Solid lines are guides to the eye. The shaded band from −0.4 nA to 0.4 nA marks the maximum noise fluctuation range. **c**, Anisotropic photocurrent response under different excitation powers at 4 μm shown in the polar plots. The incident linearly polarized light before passing through the waveplate is along the *a* axis. The polar angle is the polarization angle of the linearly polarized light with respect to the crystallographic *a* axis after passing through the half-waveplate. The experimental errors for 632.8 nm, 1,550 nm, 4 μm and 10.6 μm excitations in **a**–**c** are typically below 0.30 nA, 0.12 nA, 0.27 nA and 0.03 nA, respectively, and were obtained by calculating standard deviations of multiple measurements. **d**, Excitation power dependence of the anisotropy ratio between the photoresponses under LP-a and LP-b excitations, down to the excitation power that has a non-zero response along the crystallographic *b* axis. The horizontal axis is plotted in a log scale with the low-power region highlighted. The ratio at the low-power region is marked with a dashed red line. Experimental errors in the anisotropy ratio were obtained by taking propagation of the errors in the photocurrent response under LP-a and LP-b excitations. The maximum error is below 0.063 for an excitation power over 0.5 μW, which is not visible in the plot.

incident laser) in the C_{2v} crystallographic point group. The rank-3 tensor $\sigma_{(2)}^{\alpha\beta\gamma}$ for the d.c. optical response along the *c* axis is not zero by symmetry; however, experimentally, such an optical response is not collected efficiently by the electrodes along the *a* axis in our experimental geometry, as discussed in Supplementary Section V. The rank-4 tensors $\sigma_{(3)}^{\alpha\lambda\beta\gamma}$ that are responsible for the third-order nonlinear d.c. optical response have finite elements involving only planar components. The third-order nonlinear d.c. response necessarily involves a d.c. electric field $\mathbf{E}_{dc}$. Experimentally, $\mathbf{E}_{dc}$ can be provided by multiple effects, such as a built-in electric field due to the workfunction difference between $TaIrTe_4$ and the metal contacts, or a photothermoelectric field after photoexcitation[32,33]. The observed d.c. photocurrent is therefore seen as a result of the combination of an in-plane d.c. field $\mathbf{E}_{dc}$ arising from space charge (presumably due to the device geometry) and the optical excitation, in a third-order nonlinear process, that is, $\sigma_{(3)}^{\alpha\lambda\beta\gamma}(0,\omega,-\omega)E_{dc}^{\lambda}E_{opt}^{\beta}(\omega)E_{opt}^{\gamma}(-\omega)+\text{c.c.}$

In our approximate calculations, $\mathbf{E}_{dc}$ is treated as accelerating the Bloch electrons, displacing the Fermi distribution (see Methods). This accelerating d.c. field is then seen to place the system in a non-equilibrium state without full C_{2v} symmetry, leading to a non-zero second-order d.c. optical response. Thus, the rank-4 tensor is approximated by the second-order d.c. response with a displaced distribution due to $\mathbf{E}_{dc}$.

In accordance with the device geometry and sample orientation, $\mathbf{E}_{dc}$ is taken to be along the crystallographic *a* direction in the simulation; however, we note that $\mathbf{E}_{dc}$ can be along any other in-plane directions, for example the crystallographic *b* direction, as discussed in Supplementary Section VI, and the analysis thereafter stays qualitatively the same. Under our experimental configuration, $\sigma_{(3)}^{aaaa}$ mainly accounts for the shift current response that is measured with LP-a excitation. The 4 μm photon excitation actually involves transitions between many bands besides the two forming the Weyl cone. The representative transitions are marked in the band diagram shown in Fig. 3a. Figure 3b further shows that the contribution of $\sigma_{(3)}^{aaaa}$ from individual optical transitions across the Weyl node takes the major portion of the $\sigma_{(3)}^{aaaa}$ response under different $\mathbf{E}_{dc}$. The Weyl nodes are characterized by a divergent Berry curvature, which can be thought of like a magnetic monopole in *k*-space. Remarkably, the Berry curvature is also the curl of the Berry connection, which, along with its derivatives, determines the

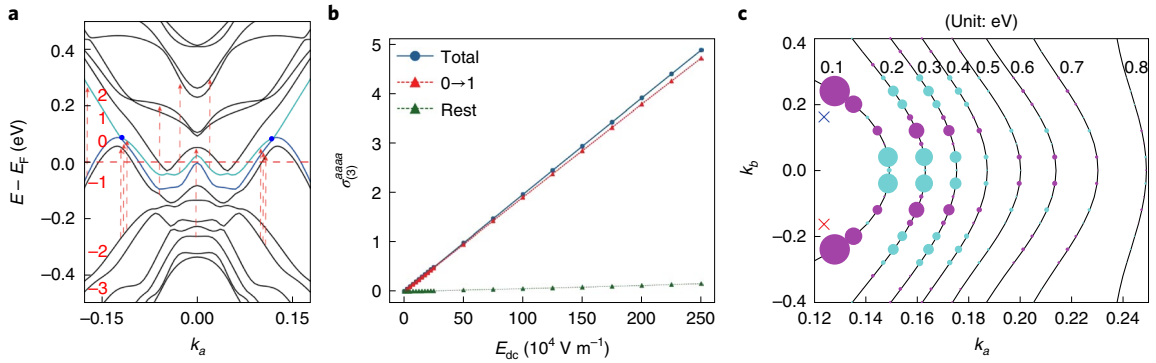

Fig. 3 | Numerical simulation of the shift current response. a, Band energy (E) dispersion cutting through a pair of Weyl nodes along the k_a direction. The red dashed line indicates the theoretically predicted Fermi level (E_F) and the red arrows indicate the possible optical transitions with 4 μm excitation. Numbers represent the band indices, and the 0th band and 1st band cross each other to form tilted Weyl cones. **b**, Third-order nonlinear tensor $\sigma^{aaaa}_{(3)}$ as a function of the built-in electric field $\mathbf{E}_{dc}$ with 4 μm optical excitation at 300 K. The solid blue line represents the total $\sigma^{aaaa}_{(3)}$, which consists of all the possible optical transitions. The dashed red line marks the contribution from the optical transition across the Weyl nodes (0→1 band) and the dashed green line is the total contribution from all other transitions. **c**, Fixed energy contour plot of the matrix elements $r^a_{mn}r^a_{nm;a} + r^a_{mn}r^a_{nm;a}$, which are the integrands of the effective third-order optical conductivity tensor at a fixed energy contour. The radius of the disc indicates the numerical value of the matrix elements and the purple (cyan) colour indicates positive (negative) sign. Red (+1) and blue (−1) crosses are Weyl points with opposite chirality.

magnitude of the nonlinear optical processes responsible for the shift current. It is therefore expected that, symmetry permitting, the Weyl fermions can generate a significant nonlinear optical response in the form of shift current, as the shift current can enjoy the same boost as the Berry curvature in the vicinity of the Weyl nodes (Fig. 3c). Indeed, after separating the photocurrent response of all optical transitions in the calculations, we found that the photocurrent response from the 4 μm transition at the Weyl cone (from band 0→1) accounts for over 97% of the photocurrent response.

According to the above shift current response scheme, the saturation behaviour observed at relatively high excitation power (~200−500 nW) with 4 μm LP-a excitation (Fig. 2a) is a result of the band filling effect in Weyl cones, as discussed theoretically in the 1D N site fermion chain model[18]. Specifically, the saturation is determined by competition between the photoabsorption rate (W_{VC}) and the relaxation mechanism (characterized by relaxation rate Γ). If $W_{VC} \ll \Gamma$, which applies in a low excitation region, the shift current is proportional to the intensity as expected, but in a high excitation region, $W_{VC} \gg \sim\Gamma$, the shift current quickly saturates and becomes independent of intensity. The photocurrent rises very quickly at low excitation power (Fig. 2b), where the shift current response dominates. The onset of a linear power dependence of the photoresponse with low responsivity is around 600 nW, where other photoresponse mechanisms such as the photothermoelectric effect dominate. We further note that the anisotropy ratio of 1.92 at high excitation power is in good agreement with the recently reported anisotropy ratio determined using d.c. conductivity measurements[34].

Besides behaviour in relation to the excitation power, the wavelength dependence of the photoresponse provides additional support to the Weyl nature of the shift current responses. As the divergence of the Berry curvature occurs in the vicinity of the Weyl cones, the responsivities at large excitation photon energies (1.55 μm and 633 nm) are as expected as the transitions are far away from the Weyl nodes (Fig. 2a). This supports that the low-power responsivity observed at 4 μm is related to the singularity of the Weyl nodes. However, for 10.6 μm excitation, the optical transitions are closer to the Weyl nodes than with 4 μm, but the responsivity at low excitation power is as expected instead of showing behaviour similar to 4 μm. This is because the transitions for 10.6 μm in the vicinity of Weyl cones are Pauli blocked and are allowed only due to the temperature smearing the Fermi surface as the temperature elevates (as described in detail in Supplementary Section VII).

Furthermore, the injection current response through other third-order nonlinear tensors $\eta^{baab}_{(3)}$ and $\eta^{baba}_{(3)}$ (Supplementary Section V) is also enhanced at 4 μm, possibly due to the same Berry curvature singularity enhancement. Experimentally, we can separate out the injection current response from the shift current response through the CPGE measurement by rotating a quarter-waveplate as described in the Methods. The excitation optical field $\mathbf{E}_{opt}(\hat{\theta})$ corresponds to an LP-a light field passing through a rotating quarter-waveplate with fast axis $\hat{\theta}$ with respect to the crystallographic a axis ($\hat{\mathbf{a}}$), and incidents to the device along the crystallographic c axis ($\hat{\mathbf{c}}$):

$$\mathbf{E}_{opt}(\hat{\theta}) = E_{opt}(\hat{\mathbf{a}})\{(\hat{\theta}\cdot\hat{\mathbf{a}})\hat{\theta} + i[(\hat{\mathbf{c}}\times\hat{\theta})\cdot\hat{\mathbf{a}}]\hat{\mathbf{c}}\times\hat{\theta}\}$$
$$= E_{opt}(\hat{\mathbf{a}})(\cos\theta\hat{\theta} - i\sin\theta\hat{\mathbf{c}}\times\hat{\theta})$$

The optical field is circularly polarized for $\theta = \pi/4$ and $3\pi/4$. As described in Supplementary Section VIII, the response from the shift tensors is dominated by the $\hat{\theta}$-independent and $\pi/2$-periodicity parts, while the response from the injection tensors contains only the π-periodicity part, which results in different responsivities under RCP and LCP excitations (Fig. 2b).

The CPGE measurement results are shown in Fig. 4 (more CPGE data are provided in Supplementary Sections IX–XII). Figure 4a shows typical results when the light spot is fixed on a negative (blue) and a positive (red) photoresponse part, respectively. The directions of the net photocurrent are opposite at these two spots; as a result, the in-plane electric field $\mathbf{E}_{dc}$ should have opposite directions. The photoresponse shows complicated polarization dependence when tuning $\hat{\theta}$ continuously. The Fourier transform from $\hat{\theta}$ space to the angular frequency space (Fig. 4b) can separate components with different angular periodicities. Apart from the low-frequency component that corresponds to the polarization-independent photocurrent response (I_∞), two sharp peaks at angular frequencies of $1/\pi$ ($I_{1/\pi}$) and $2/\pi$ ($I_{2/\pi}$) are observed. The intensity of the minor peak at an angular frequency of $1/2\pi$ represents the noise floor of the photocurrent measurement when rotating the quarter-waveplate over a 2π period. In Fig. 4c, we further show the frequency-filtered photocurrent of different periodicities. If we add I_∞, $I_{2/\pi}$ and $I_{1/\pi}$ together, we recover the experimentally measured signal shown by the solid lines in Fig. 4a. Here, $I_{2/\pi}$ corresponds to the in-plane anisotropic response and $I_{1/\pi}$ is the circular polarization-dependent component that is responsible for the injection current. Figure 4d further

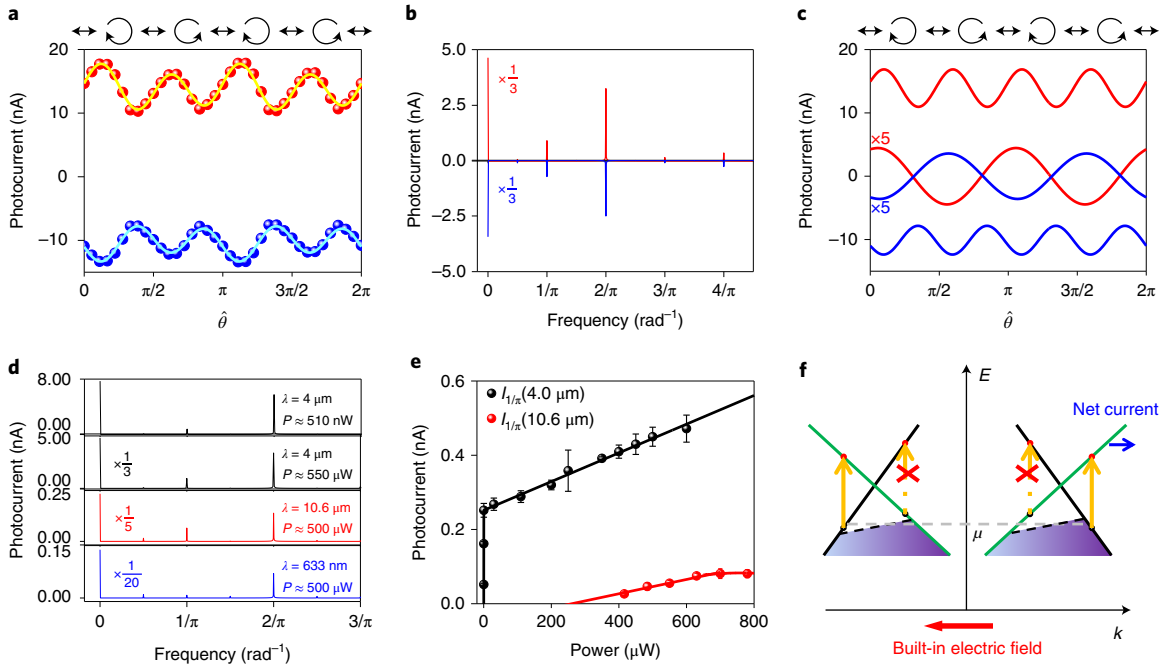

Fig. 4 | Circular photogalvanic response. a, Photocurrent response as a function of $\hat{\theta}$, the angle of the fast axis of the quarter-waveplate with respect to the polarization orientation of the incident light. The polarization direction of the incident light before passing through the quarter-waveplate has a 60° angle with respect to the crystallographic *a* axis, which accounts for the shift of the first maximum (red) or minimum (blue) from $\hat{\theta} = 0$. The measurement is performed on the positive (red dots) and negative (blue dots) photoresponse parts as marked by the red and blue circles in Fig. 1i. The excitation power is 570 μW at 4 μm. Typical experimental errors are below 0.2 nA, and were obtained by calculating standard deviations of multiple measurements. **b**, Fourier transform from $\hat{\theta}$ space to the angular frequency space. **c**, The π-periodicity ($I_{1/\pi}$) and π/2-periodicity ($I_{2/\pi}$) components from CPGE measurements of positive (red) and negative (blue) photoresponse positions. The solid lines in **a** are summations of $I_{2/\pi}$, $I_{1/\pi}$ and $\hat{\theta}$ independent components. **d**, Fourier transform spectrum of CPGE measurements with different wavelengths and excitation powers. **e**, Power dependence of $I_{1/\pi}$ under 10.6 μm and 4.0 μm excitations, respectively. Error bars are obtained by taking the 2π-periodicity components from the CPGE measurements. **f**, Schematics of the chiral selection rule and CPGE response from a pair of Weyl cones in momentum space. The grey dashed line denotes the Fermi level μ without applying a built-in electric field. Red crosses mark the forbidden transitions.

shows the wavelength-dependent CPGE measurements, where I_{∞} and $I_{2/\pi}$ components are both notable at all excitation wavelengths and the $I_{1/\pi}$ component is negligible at high-energy 633 nm photon excitation. Both 4 μm and 10.6 μm excitations result in significant $I_{1/\pi}$; however, according to the power dependence measurements of $I_{1/\pi}$ shown in Fig. 4e, $I_{1/\pi}$ has cut off at low power with 10.6 μm excitation, while it survives at very low excitation intensity down to the detection limit with 4 μm excitation. The survival of $I_{1/\pi}$ at low excitation power at 4 μm may imply enhancement of another third-order nonlinear tensor $\eta^{baba}_{(3)}$ (or $\eta^{abba}_{(3)}$) as a result of the Berry curvature singularity in the vicinity of the Weyl nodes[35].

The CPGE response ($I_{1/\pi}$) is allowed in $TaIrTe_4$ by the crystal symmetry through the third-order nonlinear tensor $\eta^{baba}_{(3)}$ ($\eta^{abba}_{(3)}$) under an in-plane $\mathbf{E}_{dc}$ along the crystallographic *a* (*b*) axis (Supplementary Section V). Similar to the shift current response, besides the transition in the vicinity of the Weyl cones, many optical transitions can account for the $I_{1/\pi}$. However, we note that the observed $I_{1/\pi}$ is probably dominated by the chiral response of the type-II Weyl cones for many reasons, as described in Supplementary Section XIII.

The CPGE response from the Weyl cone is a result of the chirality selection rule, which is illustrated in Fig. 4f. The optical transition from the lower part to the upper part of the Weyl cone is mutually determined by the chirality of the Weyl node and the excitation photon. For RCP excitation and the $\chi = +1$ Weyl fermion, the optical transition is allowed on the $+k$ side but forbidden on the $-k$ side due to the conservation of angular momentum[31,36,37]. Due to the above selection rule, RCP will result in a unidirectional current along the $+k$ direction in the $\chi = +1$ Weyl fermion, while LCP will result in a current with opposite direction. With a pair of Weyl nodes with opposite chirality and exactly the same band structure related by crystal mirror symmetry (exactly the case in $TaIrTe_4$), the net response due to the above chiral selection rule should vanish. One possible route to observe the CPGE in a WSM relies on a tilted Weyl cone and the asymmetric photoexcitation at the nodal points due to the Pauli blocking effect[36], which has been realized experimentally in type-I WSM TaAs[31]. In this work, the built-in electric field $\mathbf{E}_{dc}$ plays a role in tilting the Fermi levels between opposite-chirality Weyl nodes after photoexcitation (Supplementary Section XIV). Consequently, the imbalance of the Fermi levels will result in differently allowed momentum spaces for optical transitions at certain a photon energy crossing the Weyl cone (Supplementary Section XV). For certain circular polarization excitation, due to the imbalance of the allowed momentum space for optical transitions, the generated current from the opposite Weyl nodes cannot cancel each other and hence contribute to the net photocurrent that is transverse to the direction of $\mathbf{E}_{dc}$ as defined by $\eta^{baab}_{(3)}$ and $\eta^{baba}_{(3)}$. Although the transverse current is perpendicular to $\mathbf{E}_{dc}$, it is still detectable under our measurement scheme with its non-zero projection along the electrodes. Furthermore, if $\mathbf{E}_{dc}$ switches sign, the generated $I_{1/\pi}$ should also switch sign, which is the exact characteristic observed experimentally. The current direction of the $I_{1/\pi}$ component switches sign as the measurement is shifting from the red to blue spot when $\mathbf{E}_{dc}$ switches sign (Fig. 4c). According to this result, the in-plane $\mathbf{E}_{dc}$ provides an additional control means for chiral carriers beyond light helicities.

Finally, we note that the Berry curvature enhanced giant photoresponse has practical significance for highly sensitive photodetection applications, especially for the technically important mid-infrared and terahertz region. The un-optimized maximum room-temperature responsivity of 130.2 mA W^{-1} at 4 μm is poised to catch up with the performance of a state-of-the-art MCT (HgCdTe) detector (600 mA W^{-1}) running at low temperature[38,39]. Such an effect could potentially be much larger if the second-order instead of third-order nonlinear effect is used with materials of suitable crystal symmetry. With doping control, the highly sensitive detection could be applied over a broad wavelength range, in particular for a longer wavelength approaching the Weyl node. On the other hand, the advantage of the third-order nonlinear effect is that the in-plane electric field provides another convenient control over the chiral carrier injection beyond light helicity, which opens up experimental possibilities for studying and controlling the Weyl fermions and their associated quantum anomalies.

Online content

Any methods, additional references, Nature Research reporting summaries, source data, statements of data availability and associated accession codes are available at https://doi.org/10.1038/s41563-019-0296-5.

Received: 9 July 2018; Accepted: 23 January 2019;
Published online: 04 March 2019

References

1. Ren, Y. F., Qiao, Z. H. & Niu, Q. Topological phases in two-dimensional materials: a review. *Rep. Prog. Phys.* **79**, 066501 (2016).
2. Weng, H. M., Yu, R., Hu, X., Dai, X. & Fang, Z. Quantum anomalous Hall effect and related topological electronic states. *Adv. Phys.* **64**, 227–282 (2015).
3. Wehling, T. O., Black-Schaffer, A. M. & Balatsky, A. V. Dirac materials. *Adv. Phys.* **63**, 1–76 (2014).
4. Hosur, P. & Qi, X. L. Recent developments in transport phenomena in Weyl semimetals. *C. R. Phys.* **14**, 857–870 (2013).
5. Wan, X. G., Turner, A. M., Vishwanath, A. & Savrasov, S. Y. Topological semimetal and Fermi-arc surface states in the electronic structure of pyrochlore iridates. *Phys. Rev. B* **83**, 205101 (2011).
6. Xu, S.-Y. et al. Discovery of a Weyl fermion semimetal and topological Fermi arcs. *Science* **349**, 613–617 (2015).
7. Lv, B. Q. et al. Experimental discovery of Weyl semimetal TaAs. *Phys. Rev. X* **5**, 031013 (2015).
8. Xu, Y., Zhang, F. & Zhang, C. W. Structured Weyl points in spin–orbit coupled fermionic superfluids. *Phys. Rev. Lett.* **115**, 265304 (2015).
9. Soluyanov, A. A. et al. Type-II Weyl semimetals. *Nature* **527**, 495–498 (2015).
10. Chan, C. K., Lee, P. A., Burch, K. S., Han, J. H. & Ran, Y. When chiral photons meet chiral fermions: photoinduced anomalous Hall effects in Weyl semimetals. *Phys. Rev. Lett.* **116**, 026805 (2016).
11. Inoue, H. et al. Quasiparticle interference of the Fermi arcs and surface-bulk connectivity of a Weyl semimetal. *Science* **351**, 1184–1187 (2016).
12. Deng, K. et al. Experimental observation of topological Fermi arcs in type-II Weyl semimetal $MoTe_2$. *Nat. Phys.* **12**, 1105–1110 (2016).
13. Belopolski, I. et al. Signatures of a time-reversal symmetric Weyl semimetal with only four Weyl points. *Nat. Commun.* **8**, 942 (2017).
14. Zhang, C.-L. et al. Signatures of the Adler–Bell–Jackiw chiral anomaly in a Weyl fermion semimetal. *Nat. Commun.* **7**, 10735 (2016).
15. Huang, X. C. et al. Observation of the chiral-anomaly-induced negative magnetoresistance in 3D Weyl semimetal TaAs. *Phys. Rev. X* **5**, 031023 (2015).
16. Parameswaran, S. A., Grover, T., Abanin, D. A., Pesin, D. A. & Vishwanath, A. Probing the chiral anomaly with nonlocal transport in three-dimensional topological semimetals. *Phys. Rev. X* **4**, 031035 (2014).
17. Wu, L. et al. Giant anisotropic nonlinear optical response in transition metal monopnictide Weyl semimetals. *Nat. Phys.* **13**, 350–355 (2017).
18. Morimoto, T. & Nagaosa, N. Topological nature of nonlinear optical effects in solids. *Sci. Adv.* **2**, e1501524 (2016).
19. Osterhoudt, G. B. et al. Colossal mid-infrared bulk photovoltaic effect in a type-I Weyl semimetal. *Nat. Mater.* https://doi.org/10.1038/s41563-019-0297-4 (2019).
20. Morimoto, T., Zhong, S. D., Orenstein, J. & Moore, J. E. Semiclassical theory of nonlinear magneto-optical responses with applications to topological Dirac/Weyl semimetals. *Phys. Rev. B* **94**, 245121 (2016).
21. von Baltz, R. & Kraut, W. Theory of the bulk photovoltaic effect in pure crystals. *Phys. Rev. B* **23**, 5590–5596 (1981).
22. Sipe, J. E. & Shkrebtii, A. I. Second-order optical response in semiconductors. *Phys. Rev. B* **61**, 5337–5352 (2000).
23. Choi, T., Lee, S., Choi, Y. J., Kiryukhin, V. & Cheong, S. W. Switchable ferroelectric diode and photovoltaic effect in $BiFeO_3$. *Science* **324**, 63–66 (2009).
24. Young, S. M. & Rappe, A. M. First principles calculation of the shift current photovoltaic effect in ferroelectrics. *Phys. Rev. Lett.* **109**, 116601 (2012).
25. Young, S. M., Zheng, F. & Rappe, A. M. First-principles calculation of the bulk photovoltaic effect in bismuth ferrite. *Phys. Rev. Lett.* **109**, 236601 (2012).
26. Shi, D. et al. Low trap-state density and long carrier diffusion in organolead trihalide perovskite single crystals. *Science* **347**, 519–522 (2015).
27. de Quilettes, D. W. et al. Impact of microstructure on local carrier lifetime in perovskite solar cells. *Science* **348**, 683–686 (2015).
28. Yang, X., Burch, K. & Ran, Y. Divergent bulk photovoltaic effect in Weyl semimetals. Preprint at https://arxiv.org/abs/1712.09363 (2017).
29. Koepernik, K. et al. $TaIrTe_4$: a ternary type-II Weyl semimetal. *Phys. Rev. B* **93**, 201101 (2016).
30. Novoselov, K. S., Mishchenko, A., Carvalho, A. & Castro Neto, A. H. 2D materials and van der Waals heterostructures. *Science* **353**, aac9439 (2016).
31. Ma, Q. et al. Direct optical detection of Weyl fermion chirality in a topological semimetal. *Nat. Phys.* **13**, 842–847 (2017).
32. Gabor, N. M. et al. Hot carrier–assisted intrinsic photoresponse in graphene. *Science* **334**, 648–652 (2011).
33. Sun, D. et al. Ultrafast hot-carrier-dominated photocurrent in graphene. *Nat. Nanotechnol.* **7**, 114–118 (2012).
34. Liu, Y. N. et al. Raman signatures of broken inversion symmetry and in-plane anisotropy in type-II Weyl semimetal candidate $TaIrTe_4$. *Adv. Mater.* **30**, 1706402 (2018).
35. de Juan, F., Grushin, A. G., Morimoto, T. & Moore, J. E. Quantized circular photogalvanic effect in Weyl semimetals. *Nat. Commun.* **8**, 15995 (2017).
36. Chan, C. K., Lindner, N. H., Refael, G. & Lee, P. A. Photocurrents in Weyl semimetals. *Phys. Rev. B* **95**, 041104 (2017).
37. Yu, R., Weng, H. M., Fang, Z., Ding, H. & Dai, X. Determining the chirality of Weyl fermions from circular dichroism spectra in time-dependent angle-resolved photoemission. *Phys. Rev. B* **93**, 205133 (2016).
38. Theocharous, E., Ishii, J. & Fox, N. P. A comparison of the performance of a photovoltaic HgCdTe detector with that of large area single pixel QWIPs for infrared radiometric applications. *Infrared Phys. Technol.* **46**, 309–322 (2005).
39. Rogalski, A., Antoszewski, J. & Faraone, L. Third-generation infrared photodetector arrays. *J. Appl. Phys.* **105**, 091101 (2009).

Acknowledgements

The authors acknowledge helpful discussions with J. Sipe, R. Muniz and Q. Ma. This project was supported by the National Natural Science Foundation of China (NSFC grants nos. 91750109, 11725415, 11674013, 11774010, 11704012 and 11374021), the National Basic Research Program of China (973 grant no. 2014CB920900), the National Key Research and Development Program of China (grants nos. 2018YFA0305601, 2018YFA0305604 and 2016YFA0301004), the Recruitment Program of Global Experts and the State Key Laboratory of Precision Measurement Technology and Instruments Fund for open topics. Z.L. and P.Y. acknowledge support from the Singapore National Research Foundation under NRF award number NRF-RF2013-08, MOE Tier 2 MOE2016-T2-2-153 and MOE2017-T2-2-136. J.F. acknowledges support from the Strategic Priority Research Program of the Chinese Academy of Sciences (grant no. XDB28000000). The computations are supported by the High-performance Computing Platform of Peking University and the Tianhe-1 National Supercomputing Center in Tianjin.

Author contributions

D.S. conceived the idea and designed the experiments. Y.P. synthesized the bulk $TaIrTe_4$ materials under the supervision of Z.L. Y.L. fabricated the $TaIrTe_4$ devices under the supervision of J.-H.C. J.M., J.L. and X.Z. performed the optical measurements under the supervision of D.S. Q.G. performed the band calculations under the supervision of J.F. J.M., Q.G., J.F. and D.S. analysed the results. D.S. wrote the manuscript, assisted by J.M., Q.G., J.-H.C. and J.F. All authors commented on the manuscript.

Competing interests

The authors declare no competing interests.

Additional information

Supplementary information is available for this paper at https://doi.org/10.1038/s41563-019-0296-5.

Reprints and permissions information is available at www.nature.com/reprints.

Correspondence and requests for materials should be addressed to J.-H.C., J.F. or D.S.

Publisher's note: Springer Nature remains neutral with regard to jurisdictional claims in published maps and institutional affiliations.

Methods

Photoresponse measurement. The laser sources used in the optical measurements were two quantum cascade lasers operating at 10.6 μm and 4 μm and a HeNe laser with a continuous-wave 633 nm output. A ×50 reflective objective lens was used to focus the beam on the sample. The optical spot sizes were about 40, 10 and 1.5 μm for 10.6 μm, 4 μm and 633 nm, respectively, estimated from the scanning reflection image across a sharp edge. The sample was placed on a 2D (x–y) stage to perform spatial scanning. The photocurrent and reflection images were recorded at the same time, so the absolute location of the photoinduced signal could be found by comparison with the simultaneously taken reflection image. The light was first polarized by a linear polarizer and then the polarization was further modulated using a rotatable quarter/half-waveplate characterized by an angle θ with respect to the polarization direction of the linear polarizer. The light polarization after the quarter/half-waveplate was checked with verification measurements as described in Supplementary Sections XVI and XVII. Schematic diagrams of the linear polarization-dependent measurement achieved by rotating a half-waveplate and the CPGE measurement obtained by rotating a quarter-waveplate are shown in Supplementary Section XVIII. Throughout this Article, we assign the light propagation direction as $-\hat{\mathbf{c}}$, which is along the crystallographic c axis (perpendicular to the in-plane direction of the $TaIrTe_4$ flake).

Crystal growth and device fabrication. $TaIrTe_4$ single crystals were synthesized by solid-state reaction with the help of Te flux. All the used elements were stored and acquired in an argon-filled glovebox with moisture and oxygen levels less than 0.1 ppm, and all manipulations were carried out in the glovebox. Ta powder (99.99%), Ir powder (99.999%) and Te lump (99.999%) with an atomic ratio of Ta/Ir/Te = 1:1:12 (Sigma-Aldrich) were loaded into a quartz tube and then flame-sealed under a high vacuum of 10^{-6} torr. The quartz tube was placed in a tube furnace, slowly heated to 1,000 °C and maintained at this temperature for 100 h, and then allowed to cool to 600 °C at a rate of 0.8 °C h^{-1}, followed by cooling to room temperature. Shiny, needle-shaped $TaIrTe_4$ single crystals could be obtained from the product. Freshly exfoliated thin $TaIrTe_4$ flakes were transferred onto a 300 nm SiO_2/Si substrate. A standard electron-beam lithography technique was used to pattern electrodes consisting of 5 nm Cr and 50 nm Au on the $TaIrTe_4$ samples to form devices.

Numerical simulation of the photoresponse. To numerically calculate the photocurrent using density functional theory, the effect of $\mathbf{E}_{dc}$ on the second-order optical response was added through a shifting of the Fermi level in the momentum space using

$$f(\mathbf{k}) = f^0\left(\mathbf{k} + \frac{e\tau\mathbf{E}_{dc}}{\hbar}\right) \tag{1}$$

where τ is the momentum relaxation time, f^0 is thermal equilibrium distribution and k is the crystal quasi-momentum. The existence of a axis orientating $\mathbf{E}_{dc}$ would break the mirror symmetry along the a axis direction. In this way, we could calculate the effective third-order d.c. optical response (rank-4) tensors using

$$\begin{aligned}\sigma^{aa\beta\gamma}_{(3)R}(0,\omega,-\omega) &= -\frac{i\pi e^3}{2\hbar^2}\int\frac{d\mathbf{k}}{8\pi^3}\sum_{n,m} f_{n,m}\,(r^{\beta}_{mn}r^{\gamma}_{nm;\alpha} \\ &\quad + r^{\gamma}_{mn}r^{\beta}_{nm;\alpha})\,\delta(\omega_{mn}-\omega)\end{aligned} \tag{2}$$

$$\begin{aligned}\bar{\sigma}^{aa\beta\gamma}_{(3)I}(0,\omega,-\omega) &= \frac{ie^3}{4\hbar^2}\int\frac{d\mathbf{k}}{8\pi^3} \\ &\sum_{n,m} f_{n,m}\{r^{\beta}_{mn}r^{\gamma}_{nm;\alpha}H_{-}(\omega_{mn},\omega) + r^{\gamma}_{mn}r^{\beta}_{nm;\alpha}H_{-}(\omega_{mn},-\omega)\}\end{aligned} \tag{3}$$

$$\begin{aligned}\tilde{\sigma}^{aa\beta\gamma}_{(3)I}(0,\omega,-\omega) &= \frac{ie^3}{8\hbar^2}\int\frac{d\mathbf{k}}{8\pi^3} \\ &\sum_{n,m} f_{n,m}\,(r^{\gamma}_{nm}r^{\beta}_{mn} - r^{\beta}_{nm}r^{\gamma}_{mn})\frac{\partial H_{-}(\omega_{mn},\omega)}{\partial k^{\alpha}}\end{aligned} \tag{4}$$

where $\sigma^{aa\beta\gamma}_{(3)} = \sigma^{aa\beta\gamma}_{(3)R} + i\sigma^{aa\beta\gamma}_{(3)I}$ and $\sigma^{aa\beta\gamma}_{(3)I} = \bar{\sigma}^{aa\beta\gamma}_{(3)I} + \tilde{\sigma}^{aa\beta\gamma}_{(3)I}$. Indices α, β and γ are dummy indices and can be any direction of crystal axes a, b and c. The second index a is the direction of $\mathbf{E}_{dc}$ (the a axis direction). The right-hand side of equations 2, 3 and 4 is nothing but the definition of second-order shift current tensors with the Fermi factor $f_{n,m}$ modified by equation 1 to take into account of the effect of the a axis orientating $\mathbf{E}_{dc}$ field. If $\mathbf{E}_{dc} = 0$, the imaginary part $\sigma^{aa\beta\gamma}_{(3)I}$ vanishes. n, m are the band indices and $f_{n,m} = f_n - f_m$ is the distribution difference between the nth and mth bands. All the effects of the space charge d.c. field are taken into account by $f_{n,m}$. The factor $H_{-}(\omega_{mn},\omega) = \frac{P}{\omega_{mn}-\omega} - \frac{P}{\omega_{mn}+\omega}$, where P is the principal part. $r^{\alpha}_{mn}(\mathbf{k}) = \langle u_m(\mathbf{k})|i\partial_{k^{\alpha}}|u_n(\mathbf{k})\rangle$ measures the expectation value of the position operator in momentum space and is nothing but the Berry connection. $r^{\alpha}_{mn;\beta}$ are the generalized derivatives of r^{α}_{mn}: $r^{\alpha}_{mn;\beta} = \frac{\partial r^{\alpha}_{mn}}{\partial k^{\beta}} - i\,[A^{\beta}_{m}(\mathbf{k}) - A^{\beta}_{n}(\mathbf{k})]\,r^{\alpha}_{mn}(\mathbf{k})$, and $A^{\beta}_{m}(\mathbf{k}) = \langle u_m(\mathbf{k})|i\partial_{k\beta}|u_m(\mathbf{k})\rangle$ is the intraband Berry connection.

The shift currents induced by an incident optical field $\mathbf{E}_{opt}(t) = \mathbf{E}_{opt}(\omega)e^{-i\omega t} + \mathbf{E}_{opt}(-\omega)e^{i\omega t}$ with $\mathbf{E}_{opt}(-\omega) = \mathbf{E}_{opt}(\omega)^*$ are given by

$$\begin{aligned}\mathbf{J}^{\alpha}_{shift} &= \sigma^{aa\beta\gamma}_{(3)}(0,\omega,-\omega)E^{\beta}(\omega)E^{\gamma}(-\omega) \\ &\quad + \sigma^{aa\beta\gamma}_{(3)}(0,-\omega,\omega)E^{\beta}(-\omega)E^{\gamma}(\omega)\end{aligned} \tag{5}$$

We consider a d.c. field fixed along the crystallographic a axis. The non-zero planar components are $\sigma^{aaaa}_{(3)}$, $\sigma^{aabb}_{(3)}$, $\sigma^{baab}_{(3)}$ and $\sigma^{baba}_{(3)}$. According to equations 2, 3 and 4 $\sigma^{aa\beta\gamma}_{(3)R}$ is symmetric with respect to the interchange of the last two Cartesian components while $\sigma^{aa\beta\gamma}_{(3)I}$ is antisymmetric. Here, $\sigma^{aaaa}_{(3)}$ and $\sigma^{aabb}_{(3)}$ account for the longitudinal shift current, while $\sigma^{baab}_{(3)}$ and $\sigma^{baba}_{(3)}$ account for the transverse shift current.

As seen in equations 2, 3 and 4, the shift current is obtained by the Brillouin zone integration of the gauge-invariant quantity $\mathbf{r}^{\beta}_{mn}\mathbf{r}^{\gamma}_{nm;\alpha} + \mathbf{r}^{\gamma}_{mn}\mathbf{r}^{\beta}_{nm;\alpha}$ weighted by occupation factors and the usual energy denominator (Supplementary Section VI). Thus the nonlinear shift current depends on the non-Abelian Berry connection $\mathbf{r}_{mn}(\mathbf{k}) = \langle u_m(\mathbf{k})|i\nabla_{\mathbf{k}}|u_n(\mathbf{k})\rangle$, with $u_m(\mathbf{k})$ and $u_n(\mathbf{k})$ being the mth and nth eigenstates of the Bloch Hamiltonian at crystal momentum $\mathbf{k}$. As the Weyl nodes are monopoles of Berry curvature, the contribution to shift current is expected to be singularly large near the nodes. This analysis is based on the same physical processes invoked in the recent report of the large second harmonic generation with visible light in TaAs[17].

Our density functional theory calculations (Supplementary Section VI) enable us to calculate the Berry-phase related quantities such as the Berry connections, from which the third-order optical response [22] is computed, within the approximation outlined above. There are four non-zero planar components of rank-4 tensors for $\mathbf{E}_{dc}$ along the crystallographic a direction: $\sigma^{aaaa}_{(3)}$, $\sigma^{aabb}_{(3)}$, $\sigma^{baab}_{(3)}$ and $\sigma^{baba}_{(3)}$. The four superscripts, in the order written, correspond respectively to the direction of the current, the direction of $\mathbf{E}_{dc}$ and the two optical field directions.

The injection current tensor can be computed as

$$\begin{aligned}&\eta^{aa\beta\gamma}_{(3)}(0,\omega,-\omega) \\ &= \frac{\pi e^3}{2\hbar^2}\int\frac{d\mathbf{k}}{8\pi^3}\sum_{n,m}\Delta^{\alpha}_{mn}f_{nm}\,(r^{\gamma}_{mn}r^{\beta}_{nm} - r^{\beta}_{mn}r^{\gamma}_{nm})\delta(\omega_{mn}-\omega)\end{aligned} \tag{6}$$

The right-hand side of equation 6 is nothing but the definition of the second-order injection current tensor with Fermi factor $f_{n,m}$ modified by equation (1) to take into account the effect of the a axis orientating $\mathbf{E}_{dc}$ field. Here $\Delta^{\alpha}_{mn} = v^{\alpha}_{m} - v^{\alpha}_{n}$, and $v^{\alpha}_{m} = \left\langle u_m(\mathbf{k})\left|\frac{\partial H_{\mathbf{k}}}{\hbar\partial k^{\alpha}}\right|u_m(\mathbf{k})\right\rangle$ is the velocity. $\eta^{aa\beta\gamma}_{(3)}$ is purely imaginary and antisymmetric with respect to the interchange of the last two Cartesian components, $\eta^{aa\beta\gamma}_{(3)} = -\eta^{aa\gamma\beta}_{(3)}$. The injection current only has the transverse component.

Data availability

The data that support the plots within this paper and other findings of this study are available from the corresponding authors upon reasonable request.